THE ASTROPHYSICAL JOURNAL, 564:97–107, 2002 January 1

ENERGETICS OF TeV BLAZARS AND PHYSICAL CONSTRAINTS ON THEIR EMISSION REGIONS

MOTOKI KINO,[1,2] FUMIO TAKAHARA,[1] AND MASAAKI KUSUNOSE[3]

Received 2001 January 26; accepted 2001 September 7

ABSTRACT

Using multifrequency spectra from TeV blazars in quiescent states, we obtain the physical parameters of the emission region of blazars within the framework of the one-zone synchrotron self-Compton model. We numerically calculate the steady state energy spectra of electrons by self-consistently taking into account the effects of radiative cooling with a proper account of the Klein-Nishina effect. Here electrons are assumed to be injected with a power-law spectrum and to escape on a finite timescale, which naturally leads to the existence of a break energy scale. Although we do not use time variabilities but use a model of electron escape to constrain the size of the emission region, the resultant size turns out to be similar to that obtained based on time variabilities. Through detailed comparison of the predicted emission spectra with observations, we find that for Mrk 421, Mrk 501, and PKS 2155−304, the energy density of relativistic electrons is about an order of magnitude larger than that of magnetic fields with an uncertainty within a factor of a few.

Subject headings: BL Lacertae objects: general — gamma rays: theory — radiation mechanisms: nonthermal

1. INTRODUCTION

Blazars comprising of BL Lac objects and optically violent variable quasars are characterized by rapid time variation of the energy flux, large and variable polarization, and featureless continuum spectra (see, e.g., Urry & Padovani 1995). These characteristics are considered to be the result of beamed emission from relativistic jets seen end-on (see, e.g., Blandford & Königl 1979). The discovery of strong γ-ray emission from blazars in the GeV band by the Energetic Gamma Ray Experiment Telescope (EGRET) on the *Compton Gamma Ray Observatory* is one of the most important issues for active galactic nuclei (AGNs), because more than 60 AGNs detected by EGRET are all blazar type, and no identifications as other types of AGNs such as Seyfert galaxies have been reported (Mukherjee et al. 1997) except for a probable detection from the radio galaxy Centaurus A (Hartman et al. 1999). Multifrequency observations have revealed that broadband continuum spectra of blazars consist of two components: the low-energy component from the radio to optical/UV bands sometimes extending to the X-ray band is by synchrotron radiation, while the high-energy component from X-rays to γ-rays is due to the inverse Compton scattering of soft photons (see, e.g., Kubo et al. 1998). Various soft photon sources have been proposed ranging from synchrotron photons to photons from accretion disks, either direct or reprocessed (see, e.g., Sikora, Begelman, & Rees 1994; Inoue & Takahara 1996; Dermer & Schlickeiser 1993; Blandford & Levinson 1995; Ghisellini & Madau 1996). One of the most important aspects of multifrequency observations of blazars is to probe the energetics of relativistic jets. On this point, a few blazars from which TeV γ-rays have been detected (Mrk 421, Mrk 501, PKS 2155−304, and 1ES 2344+514) are especially important, because these TeV blazars are relatively less luminous and the pure synchrotron self-Compton model can be best applied.

Up to now, source parameters of TeV blazars have been estimated in a variety of ways (see, e.g., Bednarek & Protheroe 1997; Tavecchio, Maraschi, & Ghisellini 1998; Kataoka et al. 2000). With regard to the basic energetics, however, surprisingly little attention has been paid to the energetics of electrons, which should be the central concern for the theoretical understanding of the production and bulk acceleration of relativistic jets. Based on an analytic estimate from TeV blazar observations, one of the present authors argued that relativistic electrons dominate over magnetic fields in energy densities in relativistic jets of blazars (Takahara 1997). The purpose of this study is to estimate the energy densities more quantitatively using a numerical code that self-consistently solves for electron spectra suffering from injection, escape, and radiative cooling and photon spectra with a proper account of the Klein-Nishina effect (see, e.g., Mastichiadis & Kirk 1997; Li & Kusunose 2000). Although recent observations show that even in low-activity states γ-ray spectra extend above 1 TeV (see, e.g., Aharonian et al. 2001), in this paper we restrict our attention to the quiescent states and treat the γ-rays below 1 TeV in the first step neglecting the correction for the absorption of TeV γ-rays due to the cosmic infrared background (CIB). We shortly discuss CIB absorption effects in § 5. In future research, we will separately examine this issue including the flaring states where the γ-ray spectrum clearly extends up to 10 TeV.

The rest of the paper is organized as follows. In § 2, we introduce the synchrotron self-Compton (SSC) model, and we describe our numerical treatment for solving the kinetic equations of photons and electrons. We also show the relation between model parameters and typical observables to help the search for the parameter set of the best-fit model in numerical calculations. In § 3, we discuss the analytic estimation of the ratio of the energy density of relativistic electrons to that of magnetic fields. In § 4, we show the numerical results of spectral fitting applied to three TeV blazars, i.e., Mrk 421, Mrk 501, and PKS 2155−304. (1ES

[1] Department of Earth and Space Science, Graduate School of Science, Osaka University, Toyonaka, Osaka 560-0043, Japan; kino@vega.ess.sci.osaka-u.ac.jp, takahara@vega.ess.sci.osaka-u.ac.jp.

[2] Astronomical Institute, Graduate School of Science, Tohoku University, Aoba-ku, Sendai 980-8578, Japan; kino@astr.tohoku.ac.jp.

[3] Department of Physics, School of Science, Kwansei Gakuin University, Nishinomiya 662-8501, Japan; kusunose@kwansei.ac.jp.

2344+514 is omitted because less data are available at present.) Finally in § 5, we summarize our main results and discuss some related issues.

2. ONE-ZONE SSC MODEL

2.1. *Basic Assumptions*

Nonthermal emission from TeV blazars is divided into two components: i.e., a low-energy synchrotron component extending from radio to X-rays and a high-energy inverse Compton component extending from hard X-rays to TeV γ-rays. Here the seed photons of inverse Compton scattering are the synchrotron photons in the same emission region. This SSC model has been very successful in describing the observed multifrequency spectra (see, e.g., Jones, O'Dell, & Stein 1974; Maraschi, Ghisellini, & Celotti 1992).

Further assumptions used in the present work are that (1) the emission region is one zone with a characteristic size R and is moving at a relativistic speed β in units of the light speed and that (2) both relativistic electrons and photons are isotropic in the source frame. The beaming (Doppler) factor is given by $\delta = 1/[\Gamma(1 - \beta \cos \theta)]$, where θ is the angle between the line of sight and the direction of the relativistic jet and Γ is the bulk Lorentz factor of the emission region in the jet. When the observer lies within the angle of $\theta \sim 1/\Gamma$, we obtain $\Gamma \sim \delta$. The Hubble constant is assumed to be 75 km s^{-1} Mpc^{-1}. Throughout this paper we use these approximations.

2.2. *Numerical Approach*

Most of previous calculations are either semianalytic or done without the inverse Compton process self-consistently. In our numerical code, to obtain the consistent spectra of photons and relativistic electrons, we calculate the kinetic equations of electrons and photons self-consistently including the exact inverse Compton process within the continuous energy loss approximation.

The kinetic equation describing the time evolution of the electron distribution is given by

$$\frac{\partial n_e(\gamma, t)}{\partial t} + \frac{n_e(\gamma, t)}{t_{e,\mathrm{esc}}} = -\frac{\partial}{\partial \gamma}\left[(\dot{\gamma}_{\mathrm{syn}} + \dot{\gamma}_{\mathrm{ssc}}) n_e(\gamma, t)\right] + \mathcal{Q}_{e,\mathrm{inj}}(\gamma, t)\,, \quad (1)$$

where γ is the electron Lorentz factor and n_e is the electron number density per γ; $\dot{\gamma}_{\mathrm{syn}}$ and $\dot{\gamma}_{\mathrm{ssc}}$ are the cooling rates of synchrotron and inverse Compton emission, respectively; $t_{e,\mathrm{esc}}$ is the effective escape time of the electrons, which is identified as the timescale of the adiabatic expansion loss (Mastichiadis & Kirk 1997). For simplicity, in all the following numerical calculations, we set $t_{e,\mathrm{esc}} = 3t_{\mathrm{dyn}}$, where $t_{\mathrm{dyn}} \equiv R/c$. Next we adopt an injection spectrum

$$\mathcal{Q}_{e,\mathrm{inj}} = q_e \gamma^{-s} e^{-\gamma/\gamma_{\max}} \quad \text{for } \gamma_{\min} < \gamma\,, \quad (2)$$

where $\gamma_{\max}$ and $\gamma_{\min}$ are, respectively, the maximum and minimum Lorentz factors of the electrons, q_e is the normalization factor, and s is the power-law index. As for the injection mechanism, we implicitly assume first-order Fermi acceleration (see, e.g., Blandford & Eichler 1987). The synchrotron emissivity and absorption coefficient are calculated based on Robinson & Melrose (1984) and Crusius & Schlickeiser (1986). In the calculation of the inverse Compton scattering, we use the exact Klein-Nishina cross section and scattering probability of Jones (1968) and Coppi & Blandford (1990).

The kinetic equation of photons is given by

$$\frac{\partial n_{\mathrm{ph}}(\epsilon, t)}{\partial t} + \frac{n_{\mathrm{ph}}(\epsilon, t)}{t_{\mathrm{ph,esc}}} = \dot{n}_{\mathrm{IC}}(\epsilon, t) + \dot{n}_{\mathrm{syn}}(\epsilon, t)\,, \quad (3)$$

where ϵ is the dimensionless photon energy normalized by $m_e c^2$, with m_e being the electron mass, n_{ph} the photon number density per unit energy ϵ, and $t_{\mathrm{ph,esc}}$ the escape time of photons from the emission region, which is taken as $t_{\mathrm{ph,esc}} = R/c$ in the optically thin limit. The terms $\dot{n}_{\mathrm{IC}}(\epsilon, t)$ and $\dot{n}_{\mathrm{syn}}(\epsilon, t)$ are the production rates of inverse Compton and synchrotron photons per unit energy ϵ, respectively.

In order to obtain quiescent state spectra, calculations are performed up to $15t_{\mathrm{dyn}}$, which is long enough to reach a steady state. The physical quantities in the source frame can be converted to those in the observer frame using the relations $\epsilon_o = \epsilon_s \delta/(1 + z)$ and $dt_o = dt_s(1 + z)/\delta$, where subscripts o and s express the quantities in the observer and source frames, respectively, and z is the redshift of the source.

In this model, there are seven parameters to be determined by the comparison of predicted and observed photon spectra. They are R, the size of the emission region; B, the magnetic field strength; δ, the beaming factor; $\gamma_{\max}$, the maximum Lorentz factor; $\gamma_{\min}$, the minimum Lorentz factor; q_e, the injection rate of electrons; and s, the power-law index of the injected electron spectrum. Of them, $\gamma_{\min}$ is not easily constrained by spectral fitting, and it is taken to be 10 in all the numerical calculations. Although $\gamma_{\min}$ hardly affects the radiation spectra, it is important for probing the energy and number densities of relativistic electrons and thus the matter content of the relativistic jets, and it has been a matter of debate (see, e.g., Reynolds et al. 1996; Wardle et al. 1998; Hirotani et al. 1999). We discuss the effect of changing the value of $\gamma_{\min}$ in § 5.

2.3. *Analytic Estimate*

Before we present numerical results, we describe some analytic estimates which provide useful insight into the physics behind the relationship between the model parameters and typical observables, and we later examine quantitatively to what extent simple analytic methods are accurate. Using these relations, we construct an analytic estimate of model parameters which are then used as a starting set of parameters for numerical calculations.

2.3.1. *Relation between the Model Parameters and Observables*

Of the seven parameters, $\gamma_{\min}$ is the least constrained and is taken to be 10, as was mentioned above. The index s is determined by the spectral shape of the synchrotron radiation at low energies; specifically, the energy index α between the radio and IR bands is used to determine s by

$$s = 2\alpha + 1\,. \quad (4)$$

The other five parameters—R, B, δ, $\gamma_{\max}$, and q_e—remain to be determined. Basically, the luminosities and typical frequencies of synchrotron and inverse Compton components give four constraints. The remaining one can be taken to be the break frequency of the synchrotron radiation, which corresponds to the break Lorentz factor of electrons, γ_{br}, which results from radiative cooling before escape. In principle, the break feature may appear in the Compton component, too. However, the spectral resolution of the present γ-ray observations is not good enough. Moreover, the Klein-Nishina effect makes the situation complicated. Thus

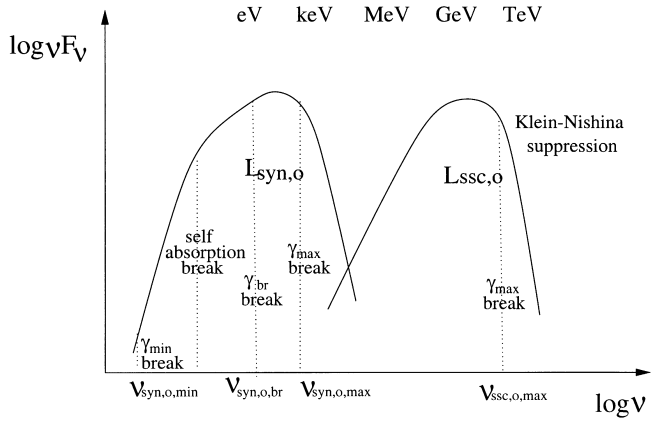

FIG. 1.—Schematic picture of the multifrequency spectrum of a typical TeV blazar. Here $L_{\mathrm{syn},o}$ and $L_{\mathrm{ssc},o}$ are the observed bolometric luminosities of synchrotron and SSC components, respectively. Corresponding to the break in the relativistic electron energy spectrum in the emission region, a break feature appears in the observed synchrotron spectrum. Around the TeV energy region, the Klein-Nishina effect suppresses the observed flux compared to the Thomson regime. We exclude the information of $\nu_{\mathrm{ssc},o,\mathrm{br}}$, because of sparse observational data points and complication from the Klein-Nishina effect.

we do not use the break frequency of the Compton component in this paper.

To sum up, the five typical observables in the observer frame are $\nu_{\mathrm{syn},o,\mathbf{max}}$, the maximum synchrotron frequency; $\nu_{\mathrm{syn},o,\mathrm{br}}$, the synchrotron break frequency; $\nu_{\mathrm{ssc},o,\mathbf{max}}$, the maximum frequency of the SSC component; $L_{\mathrm{syn},o}$, the total synchrotron luminosity; and $L_{\mathrm{ssc},o}$, the total SSC luminosity. Schematic pictures of a multifrequency radiation spectrum and a relativistic electron energy distribution are shown in Figures 1 and 2, respectively. The approximate solution of the electron kinetic equation (1) is

$$n_e(\gamma) = \begin{cases} q_e\, t_{e,\mathrm{esc}}\, \gamma^{-s} & \text{for } \gamma_{\mathbf{min}} \le \gamma < \gamma_{\mathrm{br}}\,, \\ q_e\, t_{e,\mathrm{esc}}\, \gamma_{\mathrm{br}}\, \gamma^{-s-1} & \text{for } \gamma_{\mathrm{br}} < \gamma \le \gamma_{\mathbf{max}}\,. \end{cases} \quad (5)$$

provided that $\gamma_{\mathbf{min}} < \gamma_{\mathrm{br}}$.

Using the standard formula for radiation (see, e.g., Rybicki & Lightman 1979), we can obtain five relations between the model parameters and observables. Observed

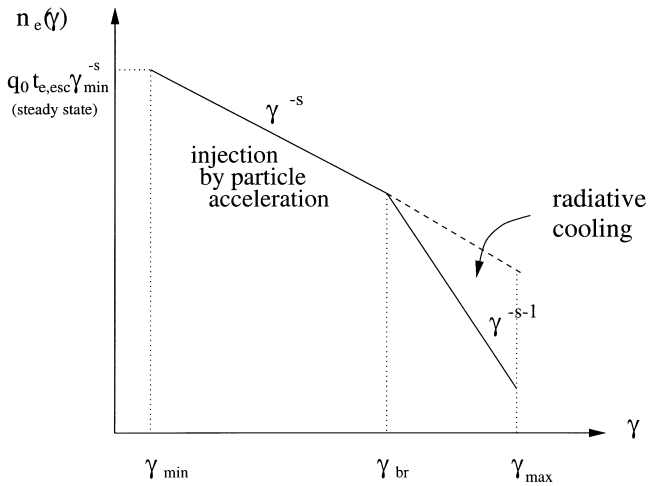

FIG. 2.—Schematic picture of the relativistic electron energy spectrum. At high Lorentz factors, radiative cooling decreases the number density of electrons and leads to a break in the spectrum.

synchrotron frequencies from a single electron of Lorentz factor γ_{br} and $\gamma_{\mathbf{max}}$ are, respectively, given by

$$\nu_{\mathrm{syn},o,\mathrm{br}} = 1.2 \times 10^6 B \gamma_{\mathrm{br}}^2 \frac{\delta}{1+z}\,, \quad (6)$$

$$\nu_{\mathrm{syn},o,\mathbf{max}} = 1.2 \times 10^6 B \gamma_{\mathbf{max}}^2 \frac{\delta}{1+z}\,. \quad (7)$$

The maximum value of the observed SSC energy in the Klein-Nishina regime is

$$h\nu_{\mathrm{ssc},o,\mathbf{max}} = C_1\, \gamma_{\mathbf{max}}\, m_e c^2 \frac{\delta}{1+z}\,, \quad (8)$$

where h is the Planck constant and $C_1 < 1$ is a constant representing the uncertainty of the Klein-Nishina effect, which typically taken to be $\frac{1}{3}$ here. It is to be noted that $h\nu_{\mathrm{ssc},o,\mathbf{max}}$ is limited by the Klein-Nishina effect unless the beaming factor is extremely large (typically larger than about 100). This is understood as follows. The detection of TeV photons means that $\gamma_{\mathbf{max}}$ is at least greater than $10^{6.5}/\delta$. If $\delta\epsilon_{\mathrm{seed},s}\gamma_{\mathbf{max}}^2 \sim 10^{12}$ eV and $\gamma_{\mathbf{max}} > 10^{6.5}/\delta$ are satisfied, we obtain $\epsilon_{\mathrm{seed},o} < 0.1\delta^2$ eV, where $\epsilon_{\mathrm{seed},s}$ and $\epsilon_{\mathrm{seed},o}$ are seed photon energies in the source frame and the observer frame, respectively. This means that the observed seed photon frequency is lower than X-ray band unless $\delta > 100$.

In the case of $s < 5/2$, bolometric synchrotron luminosity in the observer frame is given by

$$L_{\mathrm{syn},o} = 4\pi D_{\mathrm{L}}^2 F_{\mathrm{syn},o} = \frac{4\pi R^3}{3}\delta^4 \int_{\gamma_{\mathrm{br}}}^{\gamma_{\mathbf{max}}} \frac{4}{3}\sigma_{\mathrm{T}} c \gamma^2 u_B\, q_e\, t_{e,\mathrm{esc}}\, \gamma_{\mathrm{br}}\, \gamma^{-s-1} d\gamma\,, \quad (9)$$

where u_B is the energy density of magnetic fields, D_{L} is the luminosity distance, and $F_{\mathrm{syn},o}$ is the total flux of synchrotron radiation in the observer frame. Note that in the case of $s > 5/2$, the luminosity from electrons with $\gamma_{\mathbf{min}} < \gamma < \gamma_{\mathrm{br}}$ is larger than that from electrons with $\gamma_{\mathrm{br}} < \gamma < \gamma_{\mathbf{max}}$ and equation (9) is not valid. The bolometric Compton luminosity is written in a similar way, by replacing u_B by the energy density of soft photons and multiplying a suppression factor of C_2 mentioned below. The energy density of synchrotron photons is given by

$$L_{\mathrm{syn},o} = \frac{4\pi R^2}{3} c\delta^4 u_{\mathrm{syn}}\,, \quad (10)$$

when we set the photon escape time as R/c. It is important to note that because of the Klein-Nishina suppression, only photons with energy less than $m_e c^2/\gamma$ in the source frame contribute to SSC luminosity. Here, we simply denote this suppression factor by C_2. The ratio of the synchrotron and SSC luminosities is then given by

$$\frac{L_{\mathrm{syn},o}}{L_{\mathrm{ssc},o}} = \frac{u_B}{C_2\, u_{\mathrm{syn}}}\,. \quad (11)$$

The break Lorentz factor is determined by the condition that $t_{e,\mathrm{esc}}$ is equal to t_{cool}:

$$\frac{R}{C_3 c} = \frac{3 m_e c}{4(u_B + C_2\, u_{\mathrm{syn}})\sigma_{\mathrm{T}}\gamma_{\mathrm{br}}}\,, \quad (12)$$

where we set $C_3\, t_{e,\mathrm{esc}} = t_{\mathrm{dyn}}$ and assume $C_3 = \frac{1}{3}$ as has been noted in the previous subsection. This is a different approach from most of the previous work where the time

TABLE 1

MRK 421 PHYSICAL PARAMETERS FROM SSC ANALYSIS

Parameter	High Injection	Best Fit	Low Injection
δ	15.9	12	9.1
R (cm)	5.3×10^{15}	2.8×10^{16}	1.4×10^{17}
B (G)	0.44	0.12	0.036
$\gamma_{\max}$	8.3×10^{4}	1.5×10^{5}	3.45×10^{5}
s	1.6	1.6	1.6
q_e (cm^{-3} s^{-1})[a]	4.9×10^{-4}	9.6×10^{-6}	1.9×10^{-7}
$n_e^{\rm tot}$ (cm^{-3})[a,b]	1.1×10^{2}	1.1×10^{1}	1.1
$\langle\gamma\rangle$[b]	2.3×10^{2}	3.1×10^{2}	4.3×10^{2}
$\tau_{\gamma\gamma}^{c}$	8.9×10^{-3}	6.9×10^{-3}	5.5×10^{-3}
$L_{{\rm syn},o}$ (ergs s^{-1})	1.3×10^{45}	1.3×10^{45}	1.4×10^{45}
$L_{{\rm ssc},o}$ (ergs s^{-1})	0.5×10^{45}	0.7×10^{45}	0.9×10^{45}
$L_{{\rm syn+ssc},o}$ (ergs s^{-1})...	1.8×10^{45}	2.0×10^{45}	2.3×10^{45}
$L_{\rm Poy}$ (ergs s^{-1})	6.9×10^{42}	8.1×10^{42}	1.0×10^{43}
$L_{e,{\rm kin}}$ (ergs s^{-1})	1.8×10^{43}	4.0×10^{43}	7.8×10^{43}
$L_{\rm syn+ssc}$ (ergs s^{-1})	7.2×10^{42}	1.4×10^{43}	2.8×10^{43}
$L_{p,{\rm kin}}$ (ergs s^{-1})[d]	1.5×10^{44}	2.4×10^{44}	3.3×10^{44}
$L_{e,{\rm kin}}/L_{\rm Poy} = u_e/u_B$	3	5	8

[a] $\gamma_{\min}$ is fixed at 10.
[b] $n_e^{\rm tot}$ and $\langle\gamma\rangle$ are the total number density and the average Lorentz factor of relativistic electrons, respectively.
[c] $\nu L_\nu \simeq 1.3 \times 10^{44}$ ergs s^{-1} at 0.3 keV is adopted in calculating $\tau_{\gamma\gamma}$.
[d] $L_{p,{\rm kin}}$ is calculated assuming that the cold proton number density is the same as that of relativistic electrons.

variability constraint $R \sim \delta c t_{\rm var}$ is used. We think it more appropriate to avoid the time variability constraint in the case of quiescent states because the shortest time variability such as a 15 minute TeV flare (Gaidos et al. 1996) might be correlated to local regions such as a shock front (Kirk, Rieger, & Mastichiadis 1998).

2.3.2. *Analytic Estimate of Physical Parameters*

In this subsection, we analytically estimate the model parameters using the typical observables of TeV blazars. Observed total flux, typical frequencies, and luminosity distance are scaled as

TABLE 2

MRK 501 PHYSICAL PARAMETERS FROM SSC ANALYSIS

Parameter	High Injection	Best Fit	Low Injection
δ	14.5	11	8.3
R (cm)	2.0×10^{15}	1.0×10^{16}	5.3×10^{16}
B (G)	0.69	0.20	0.059
$\gamma_{\max}$	9.0×10^{4}	2.0×10^{5}	3.8×10^{5}
s	1.8	1.8	1.8
q_e (cm^{-3} s^{-1})[a]	8.7×10^{-2}	1.7×10^{-3}	3.4×10^{-5}
$n_e^{\rm tot}$ (cm^{-3})[a,b]	3.4×10^{3}	3.4×10^{2}	3.6×10^{1}
$\langle\gamma\rangle$[b]	1.0×10^{2}	1.2×10^{2}	1.5×10^{2}
$\tau_{\gamma\gamma}^{c}$	2.2×10^{-2}	1.8×10^{-2}	1.2×10^{-2}
$L_{{\rm syn},o}$ (ergs s^{-1})	8.3×10^{44}	7.8×10^{44}	8.2×10^{44}
$L_{{\rm ssc},o}$ (ergs s^{-1})	9.9×10^{44}	1.0×10^{45}	1.2×10^{45}
$L_{{\rm syn+ssc},o}$ (ergs s^{-1})...	1.8×10^{45}	1.8×10^{45}	2.0×10^{45}
$L_{\rm Poy}$ (ergs s^{-1})	2.0×10^{42}	2.4×10^{42}	3.4×10^{42}
$L_{e,{\rm kin}}$ (ergs s^{-1})	3.0×10^{43}	5.2×10^{43}	1.1×10^{44}
$L_{\rm syn+ssc}$ (ergs s^{-1})	8.6×10^{42}	1.5×10^{43}	2.9×10^{43}
$L_{p,{\rm kin}}$ (ergs s^{-1})[d]	5.2×10^{44}	7.8×10^{44}	1.3×10^{45}
$L_{e,{\rm kin}}/L_{\rm Poy} = u_e/u_B$	15	22	32

[a] $\gamma_{\min}$ is fixed at 10.
[b] $n_e^{\rm tot}$ and $\langle\gamma\rangle$ are the total number density and the average Lorentz factor of relativistic electrons, respectively.
[c] $\nu L_\nu \simeq 7.9 \times 10^{43}$ ergs s^{-1} at 0.3 keV is adopted in calculating $\tau_{\gamma\gamma}$.
[d] $L_{p,{\rm kin}}$ is calculated assuming that the cold proton number density is the same as that of relativistic electrons.

TABLE 3

PKS 2155−304 PHYSICAL PARAMETERS FROM SSC ANALYSIS

Parameter	High Injection	Best Fit	Low Injection
δ	43.6	33	25.0
R (cm)	1.9×10^{15}	9.0×10^{15}	4.5×10^{16}
B (G)	1.1	0.30	0.089
$\gamma_{\max}$	2.3×10^{4}	5.0×10^{4}	9.8×10^{4}
s	1.4	1.4	1.4
q_e (cm^{-3} s^{-1})[a]	1.4×10^{-3}	2.8×10^{-5}	5.6×10^{-7}
$n_e^{\rm tot}$ (cm^{-3})[a,b]	2.5×10^{2}	2.4×10^{1}	2.3
$\langle\gamma\rangle$[b]	2.9×10^{2}	4.8×10^{2}	7.3×10^{2}
$\tau_{\gamma\gamma}^{c}$	5.4×10^{-3}	4.6×10^{-3}	3.7×10^{-3}
$L_{{\rm syn},o}$ (ergs s^{-1})	3.4×10^{46}	3.2×10^{46}	3.4×10^{46}
$L_{{\rm ssc},o}$ (ergs s^{-1})	1.1×10^{46}	1.5×10^{46}	2.0×10^{46}
$L_{{\rm syn+ssc},o}$ (ergs s^{-1})...	4.5×10^{46}	4.7×10^{46}	5.4×10^{46}
$L_{\rm Poy}$ (ergs s^{-1})	4.1×10^{43}	4.0×10^{43}	4.9×10^{43}
$L_{e,{\rm kin}}$ (ergs s^{-1})	5.2×10^{43}	1.0×10^{44}	2.2×10^{44}
$L_{\rm syn+ssc}$ (ergs s^{-1})	2.4×10^{43}	4.3×10^{43}	8.7×10^{43}
$L_{p,{\rm kin}}$ (ergs s^{-1})[d]	3.3×10^{44}	4.0×10^{44}	5.7×10^{44}
$L_{e,{\rm kin}}/L_{\rm Poy} = u_e/u_B$	1	3	4

[a] $\gamma_{\min}$ is fixed at 10.
[b] $n_e^{\rm tot}$ and $\langle\gamma\rangle$ are the total number density and the average Lorentz factor of relativistic electrons, respectively.
[c] $\nu L_\nu \simeq 4.1 \times 10^{45}$ ergs s^{-1} at 0.3 keV is adopted in calculating $\tau_{\gamma\gamma}$.
[d] $L_{p,{\rm kin}}$ is calculated assuming that the cold proton number density is the same as that of relativistic electrons.

$$f_{\rm syn} = \frac{F_{{\rm syn},o}}{10^{-10}\ {\rm ergs\ cm^{-2}\ s^{-1}}}\,,$$

$$f_{\rm ssc} = \frac{F_{{\rm ssc},o}}{10^{-10}\ {\rm ergs\ cm^{-2}\ s^{-1}}}\,, \tag{13}$$

$$\nu_{\rm br} = \frac{\nu_{{\rm syn},o,{\rm br}}}{10^{15}\ {\rm Hz}}\,, \quad \nu_{\max} = \frac{\nu_{{\rm syn},o,\max}}{10^{17}\ {\rm Hz}}\,, \quad \nu_{\rm ssc} = \frac{\nu_{{\rm ssc},o,\max}}{10^{26}\ {\rm Hz}}\,, \tag{14}$$

and

$$d = \frac{D_{\rm L}}{100\ {\rm Mpc}}\,, \tag{15}$$

respectively. The numerical factors C_1, C_2, and C_3 normalized by $\frac{1}{3}$ are denoted by c_1, c_2, and c_3, respectively.

In order to express the model parameters in terms of the observables, first we solve five algebraic equations (6), (7), (8), (11), and (12) to obtain the five quantities R, B, δ, $\gamma_{\rm br}$, and $\gamma_{\max}$, and then by inserting them into equation (9), we obtain q_e. As a result, we obtain the typical values of parameters for TeV blazars as the following:

$$\delta = 8.9 f_{\rm syn}^{1/2}\, f_{\rm ssc}^{-1/4}\, \eta^{1/2} \nu_{\rm br}^{1/4}\, \nu_{\max}^{1/4}\, \nu_{\rm ssc}^{-1/2} \times d^{1/2} c_1^{1/2}\, c_2^{1/4}\, c_3^{-1/2}\,, \tag{16}$$

$$B = 0.13 f_{\rm syn}^{1/2}\, f_{\rm ssc}^{-1/4}\, \eta^{1/2} \nu_{\rm br}^{1/4}\, \nu_{\max}^{5/4}\, \nu_{\rm ssc}^{-5/2} \times d^{1/2} (1+z)^{-1} c_1^{5/2}\, c_2^{1/4}\, c_3^{-1/2}\ {\rm G}\,, \tag{17}$$

$$\gamma_{\rm br} = 2.7 \times 10^{4} f_{\rm syn}^{-1/2}\, f_{\rm ssc}^{1/4}\, \eta^{-1/2} \nu_{\rm br}^{1/4}\, \nu_{\max}^{-3/4}\, \nu_{\rm ssc}^{3/2} \times d^{-1/2} (1+z) c_1^{-3/2}\, c_2^{-1/4}\, c_3^{1/2}\,, \tag{18}$$

$$\gamma_{\max} = 2.7 \times 10^{5} f_{\rm syn}^{-1/2}\, f_{\rm ssc}^{1/4}\, \eta^{-1/2} \nu_{\rm br}^{-1/4}\, \nu_{\max}^{-1/4}\, \nu_{\rm ssc}^{3/2} \times d^{-1/2} (1+z) c_1^{-3/2}\, c_2^{-1/4}\, c_3^{1/2}\,, \tag{19}$$

$$R = 9.0 \times 10^{15} f_{\rm syn}^{-1/2} f_{\rm ssc}^{1/4} \eta^{-3/2} \nu_{\rm br}^{-3/4} \nu_{\rm max}^{-7/4} \nu_{\rm ssc}^{7/2} \times d^{-1/2}(1+z) c_1^{-7/2} c_2^{-1/4} c_3^{3/2} \ {\rm cm} , \quad (20)$$

$$q_e \int_{\gamma_{\rm br}}^{\gamma_{\rm max}} \gamma^{-s+1} d\gamma = 0.015 f_{\rm syn}^{1/2} f_{\rm ssc}^{1/4} \eta^{7/2} \nu_{\rm br}^{5/4} \times \nu_{\rm max}^{17/4} \nu_{\rm ssc}^{-17/2} d^{3/2}(1+z)^{-3} \times c_1^{17/2} c_2^{-1/4} c_3^{-5/2} \ {\rm cm}^{-3} \ {\rm s}^{-1} , \quad (21)$$

where $\eta = (1 + F_{{\rm ssc},o}/F_{{\rm syn},o})/2$. Here we emphasize that these expressions give a complete set of model parameters in terms of the observables and that typical numerical values turn out to be similar to those obtained in various other ways (see, e.g., Tavecchio et al. 1998; Kataoka et al. 2000). In particular, the obtained size seems to be similar to that based on time variability, which means that the size of the emission region in quiescent states is compatible with that obtained by the time variability constraint. It is seen that R and q_e have a strong dependence on $\nu_{\rm max}$ and $\nu_{\rm ssc}$ and that a variation of $\nu_{\rm ssc}$ by a factor of 2 leads to a variation of R, B, and q_e by a few orders of magnitude. Despite this, a quite robust estimate is possible for some of the quantities such as the ratio of the energy density of electrons to that of magnetic fields, as will be shown in the next section.

Although our method is model dependent in that we use a simple model of electron injection, escape, and cooling, this model is quite general and has an advantage of self-consistent treatment of the break Lorentz factor of electrons. If one does not use this relation and tries to proceed based on observables alone, one needs to introduce the electron number density instead of the injection parameter q_e and to use the time variability constraint. Most of the previous work adopted such methods and searched for suitable parameters in a two-dimensional parameter such as the (log B, log δ)-plane (see, e.g., Tavecchio et al. 1998; Bednarek & Protheroe 1997; Kataoka et al. 1999) by allowing some degree of uncertainties of the time variability constraint.

Next we check an additional constraint on the transparency of γ-rays against the intrinsic absorption: i.e., the optical depth of a γ-ray photon for pair production should be smaller than unity. For a γ-ray photon of the observed energy $\epsilon_{\gamma,o}$, the observed energy of the target photon $\epsilon_{{\rm t},o}$ is about

$$\epsilon_{{\rm t},o} = \frac{\delta}{1+z} \epsilon_{{\rm t},s} = \frac{4 m_e^2 c^4}{\epsilon_{\gamma,o}} \left(\frac{\delta}{1+z} \right)^2 . \quad (22)$$

We approximate the number density of target photons by

$$n_{t,s} = \frac{3 L_{t,s}}{4\pi R^2 c \epsilon_{t,s}} . \quad (23)$$

Then, the optical depth is given by (von Montigny et al. 1995)

$$\tau_{\gamma\gamma}(\epsilon_\gamma) = \frac{15}{256\pi} \frac{1+z}{\delta^5} \frac{\epsilon_{\gamma,o} L_{t,o} \sigma_{\rm T}}{R m_e^2 c^5} = 9.9 \times 10^{-2} \frac{L_{t,o}}{10^{44} \ {\rm ergs \ s^{-1}}} \frac{\epsilon_{\gamma,o}}{\rm TeV} \times \left(\frac{R}{10^{16} \ {\rm cm}} \right)^{-1} \left(\frac{\delta}{10} \right)^{-5} (1+z) . \quad (24)$$

If we use the typical observables, the optical depth is expressed as

$$\tau_{\gamma\gamma}(\epsilon_\gamma) = 9.8 \times 10^{-2} \frac{L_{t,o}}{L_{{\rm syn},o}} f_{\rm syn}^{-1} f_{\rm ssc} \eta^{-1} \nu_{\rm br}^{-1/2} \nu_{\rm max}^{1/2} \times (1+z)^{-5} c_1 c_2^{-1} c_3 \frac{\epsilon_{\gamma,o}}{h \nu_{{\rm ssc},o,{\rm max}}} . \quad (25)$$

Thus we find that the intrinsic absorption of 0.35 TeV photons is not so large for TeV blazars in quiescent states, but it may be important for some cases. In § 4, we will show the value for numerical solutions in Tables 1, 2, and 3.

3. ENERGY DENSITY OF RELATIVISTIC ELECTRONS AND MAGNETIC FIELD

In this section, following the methods of Takahara (1997), we show that we can analytically estimate the ratio of u_B to u_e fairly robustly. The energy density of relativistic electrons is given by

$$u_e = \int_{\gamma_{\rm min}}^{\gamma_{\rm max}} \gamma m_e c^2 n_e(\gamma) d\gamma \simeq q_e t_{e,{\rm esc}} m_e c^2 \int_{\gamma_{\rm min}}^{\gamma_{\rm br}} \gamma^{-s+1} d\gamma = 1.1 \times 10^{-2} f_{\rm ssc}^{1/2} \eta^2 \nu_{\rm br}^{1/2} \nu_{\rm max}^{5/2} \nu_{\rm ssc}^{-5} d(1+z)^{-2} \times c_1^5 c_2^{-1/2} c_3^{-2} \frac{\int_{\gamma_{\rm min}}^{\gamma_{\rm br}} \gamma^{-s+1} d\gamma}{\int_{\gamma_{\rm br}}^{\gamma_{\rm max}} \gamma^{-s+1} d\gamma} \ {\rm ergs \ cm^{-3}} , \quad (26)$$

in the framework of the previous section. The energy density of magnetic fields is also given by

$$u_B = 6.3 \times 10^{-4} f_{\rm syn} f_{\rm ssc}^{-1/2} \eta \nu_{\rm br}^{1/2} \nu_{\rm max}^{5/2} \nu_{\rm ssc}^{-5} \times d(1+z)^{-2} c_1^5 c_2^{1/2} c_3^{-1} \ {\rm ergs \ cm^{-3}} . \quad (27)$$

Although both energy densities have a fairly strong dependence on some observables, the ratio turns out to be as simple as

$$\frac{u_e}{u_B} = 9 c_2^{-1} c_3^{-1} \left(1 + \frac{f_{\rm ssc}}{f_{\rm syn}} \right) \frac{f_{\rm ssc}}{f_{\rm syn}} \frac{\int_{\gamma_{\rm min}}^{\gamma_{\rm br}} \gamma^{-s+1} d\gamma}{\int_{\gamma_{\rm br}}^{\gamma_{\rm max}} \gamma^{-s+1} d\gamma} . \quad (28)$$

Note that the strong dependence on quantities such as $\nu_{\rm ssc}$, $\nu_{\rm max}$, and c_1 in u_e and u_B are canceled out. In addition, we can derive equation (28) in a more transparent way as follows. The total radiation power is simply given by

$$L_{{\rm syn},o} + L_{{\rm ssc},o} = \tfrac{4}{3} \pi R^3 \delta^4 m_e c^2 q_e \int_{\gamma_{\rm br}}^{\gamma_{\rm max}} \gamma^{-s+1} d\gamma . \quad (29)$$

Combining equations (10), (11), (26), and (29) we can easily obtain equation (28) (the factor 9 in eq. [28] comes from the normalization of C_2 and C_3). This analytic estimation is quite useful to understand the relation between the typical observables of TeV blazars and the ratio of u_e/u_B. Needless to say, the ratio of $\gamma_{\rm br}$ to $\gamma_{\rm max}$ is obtained from the observed ratio of $\nu_{{\rm syn},o,{\rm br}}$ to $\nu_{{\rm syn},o,{\rm max}}$ (eqs. [6] and [7]). The ratio of $\gamma_{\rm br}$ to $\gamma_{\rm min}$ depends on the adopted value of $\gamma_{\rm min}$. When the synchrotron luminosity dominates over the SSC luminosity, $u_{\rm syn} \ll u_B$ and $u_e/u_B \propto f_{\rm ssc}/f_{\rm syn} \ll 1$. When the SSC luminosity dominates over the synchrotron luminosity, $u_{\rm syn} \gg u_B$ and $u_e/u_B \propto f_{\rm ssc}^2/f_{\rm syn}^2 \gg 1$. Hence, as the value of $f_{\rm ssc}/f_{\rm syn}$ increases, the value of u_e/u_B increases. Very roughly, the

equipartition between electrons and magnetic fields corresponds to sources for the SSC luminosity equal to the synchrotron luminosity, if we ignore other numerical factors such as c_2 and c_3. According to equation (28), a more realistic estimate indicates that when the SSC luminosity is equal to the synchrotron one, u_e/u_B takes a value on the order of 10.

Since the above estimate depends on several numerical factors, we should carefully examine these subtleties. As for the value of C_2, the energy of seed photons for γ-rays of $\epsilon_{\gamma,o}$ TeV is lower than about $10\epsilon_{\gamma,o}^{-1}$ eV for a typical value of $\delta = 10$. Because of the Klein-Nishina effect, synchrotron photons whose energy is higher than this value are not available to inverse Compton scattering. Thus, C_2 is expected to be less than 0.3. As for C_3, since electron escape may be identified with the expansion velocity in the downstream region of the shock, $\frac{1}{3}$ is also a reasonable guess; higher values approaching 1 requires electrons to escape as rapidly as photons, which seems to be difficult to realize. The typical ratio of $\gamma_{\rm max}$ to $\gamma_{\rm br}$ is 10. Even if this ratio is 100, u_e/u_B decreases only by a factor of a few when $s = 2$. An increase in the value of $\gamma_{\rm min}$ by a factor of 10 will decrease u_e/u_B by a factor of a few for $s = 2$. Thus, only when both $\gamma_{\rm min}$ and $\gamma_{\rm max}/\gamma_{\rm br}$ are larger than 100 can u_B be comparable to u_e. We should note that since $\gamma_{\rm min}$ is expected to be comparable with the value of the bulk Lorentz factor in the shock acceleration picture, $\gamma_{\rm min} = 10$ is a reasonable choice when the jet material consists of mainly electron-positron pairs or when electrons and ions are separately thermalized for normal plasmas (for further discussion, see § 5).

Thus, the only major uncertainty in estimating u_B/u_e is the electron index s. In a previous work, Takahara (1997) examined the case of $s = 2$ because this is the universal index expected for the nonrelativistic case (see, e.g., Blandford & Eichler 1987). In the present work, we allow this value to be less than 2, which better fits the emission spectra.

When s is smaller, u_e/u_B becomes smaller. In Figure 3 we show the resultant ratio u_e/u_B as a function of $\gamma_{\rm br}$ for several values of s. For simplicity, other parameters are fixed at $f_{\rm syn} = 1$, $f_{\rm ssc} = 1$, $\gamma_{\rm max} = 1 \times 10^5$, $\gamma_{\rm min} = 10$, $c_1 = 1$, $c_2 = 1$, and $c_3 = 1$. Figure 3 shows that even when s is as small as 1.4, u_e is larger than u_B, unless $\gamma_{\rm br}$ is smaller than 10^3. Thus, the conclusion that u_e is about 1 order of magnitude larger than u_B is fairly robust.

Before we present detailed numerical results, we describe straightforward relations between the energy densities and power carried by relativistic jets. It should be noted that the energy density of the ith radiation component (the index i corresponds to synchrotron or SSC) u_i is related to the power L_i as

$$L_i = \tfrac{4}{3}\pi R^2 c u_i \Gamma^2 , \tag{30}$$

where the factor 4/3 accounts for pressure of relativistic matter and we assume $\Gamma \gg 1$. It is worth noting that the observed luminosity is given by

$$L_{{\rm i},o} = \tfrac{4}{3}\pi R^2 c u_i \delta^4 \tag{31}$$

in the observer frame. Hence the actual radiation power is smaller than the observed luminosity by a factor of δ^2 assuming $\Gamma \sim \delta$. Similarly, the Poynting power is given by

$$L_{\rm Poy} = \tfrac{4}{3}\pi R^2 c u_B \Gamma^2 , \tag{32}$$

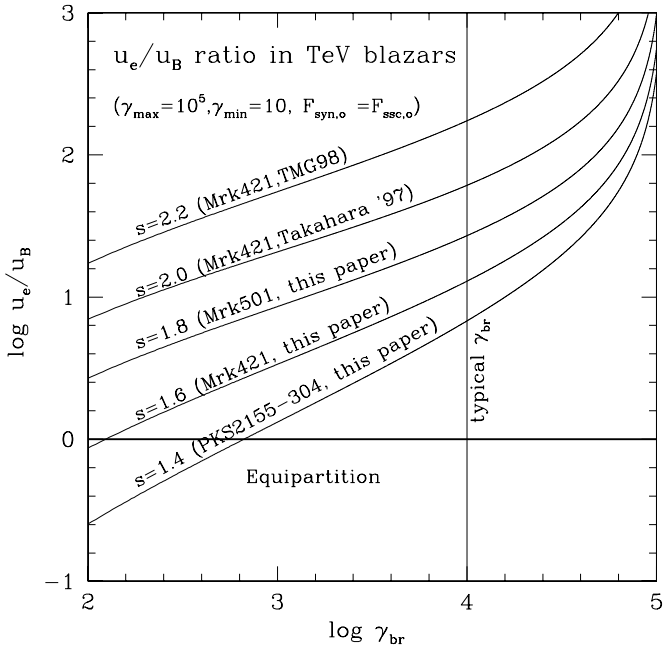

FIG. 3.—Ratio u_e/u_B in TeV blazars. This is calculated according to eq. (28). For a TeV blazar u_e is typically about 1 order of magnitude larger than u_B. We confirm this analytic result by numerical calculations. The discrepancies between this analytic estimation and numerical results are at most within a factor of a few.

and the kinetic power of relativistic electrons is

$$L_{e,\rm kin} = \tfrac{4}{3}\pi R^2 c u_e \Gamma^2 . \tag{33}$$

Thus, the discussion on the ratio u_e/u_B is straightforwardly translated into the ratio $L_{e,\rm kin}/L_{\rm Poy}$. It should be stressed that $L_{e,\rm kin}$ takes account of only relativistic electrons. In other words, the contribution from thermal electrons, which should constitute a reservoir for acceleration and that of protons, either relativistic or cold, are completely neglected. We emphasize that if we take these components into account, it is clear that kinetic power is more dominant, at least in the emission region of TeV blazars.

4. NUMERICAL RESULTS

Here we present numerical results by solving the kinetic equations and searching for best-fit model parameters for three TeV blazars (Mrk 421, Mrk 501, and PKS 2155−304). The search is made using the parameters determined analytically in the previous section. The observed values are taken from those compiled by Kataoka (2000). In his paper, the multifrequency observed spectrum is fitted with a polynomial function of the form of $\log(\nu L_\nu) = a + b \log \nu + c(\log \nu)^2 + d(\log \nu)^3$, where a, b, c, and d are the fitting constants (Comastri, Molendi, & Ghisellini 1995). Kataoka (2000) identified $\nu_{{\rm syn},o,{\rm br}}$ and $\nu_{{\rm syn},o,{\rm max}}$ as the frequencies where synchrotron luminosity reaches one-half of its peak value: the lower one is identified as $\nu_{{\rm syn},o,{\rm br}}$ and the higher one is identified as $\nu_{{\rm syn},o,{\rm max}}$. In the same way, $\nu_{{\rm ssc},o,{\rm max}}$ can be defined. However, since the spectra of high-energy γ-rays are not so well covered, we do not put a heavy weight on his determination of $\nu_{{\rm ssc},o,{\rm max}}$, but we simply assume $\nu_{{\rm ssc},o,{\rm max}} = 1 \times 10^{26}$ Hz as a starting point. It should be noted that these observables are not derived from the spectral fitting described in the previous section, but

from the polynomial fitting, so the chosen values of the model parameters above are expected to deviate from our definition by some factor.

Moreover, taking the sparseness and uncertainties of the observed data into consideration, it is natural to think some range of uncertainties are included in the model parameters, too. Such uncertainties are also investigated in this section. Here we explain the procedure of searching these parameter sets. The range of uncertainties is different for each model parameter. Of the seven model parameters, the index s can be regarded as fixed. In contrast, R and q_e are expected to have a large uncertainty, while δ is relatively stable. The search for model parameters is made as follows. We first choose a certain value of q_e. Then, we adopt a suitable value of R so as to reproduce the low-energy spectrum of the synchrotron component, whereby some discrepancies will appear at the high-energy part of the synchrotron component. Noting that the observed ratio of $L_{\mathrm{ssc},o}/L_{\mathrm{syn},o}$ is determined by the combination of $B^2\delta^4R^2$, we can adjust the break feature of the synchrotron spectrum by adopting a suitable combination of B and δ. A slight adjustment of the value of R is also made. Finally, the high-energy end of the synchrotron component is adjusted by adopting a suitable γ_{max}. In this step, slight adjustment of the model parameters that are determined in the previous steps is also made. The resultant spectral shape of the SSC component should be compared with observation, while the calculated SSC luminosity should match the observation. This comparison determines whether the chosen parameter set is allowable or not. The whole step is repeated starting from a different value of q_e to find the best-fit model parameters and uncertainties. Although this is not a complete survey of the parameter space, we believe that this provides a reasonable estimate of the uncertainties because the most uncertain parameters are q_e and R.

4.1. *Best-Fit Parameters*

4.1.1. *Mrk 421*

Mrk 421 ($z = 0.031$) is a well-known BL Lac object and the first identified source of TeV gamma-ray emission by the Whipple Cerenkov telescope (Punch et al. 1992).

Following Kataoka (2000), the observables of Mrk 421 are chosen as follows: $\alpha = 0.3$, $\nu_{\mathrm{syn},o,\mathrm{br}} = 2.5 \times 10^{14}$ Hz, $\nu_{\mathrm{syn},o,\mathrm{max}} = 1.6 \times 10^{17}$ Hz, $\nu_{\mathrm{ssc},o,\mathrm{max}} = 1.0 \times 10^{26}$ Hz, $F_{\mathrm{syn},o} = 8.6 \times 10^{-10}$ ergs cm^{-2} s^{-1}, and $F_{\mathrm{ssc},o} = 3.4 \times 10^{-10}$ ergs cm^{-2} s^{-1}. Substituting these observables into the analytic estimate described in § 2, we obtain $\delta = 14.3$, $R = 7.9 \times 10^{15}$ cm, $B = 0.31$ G, $\gamma_{\mathrm{br}} = 0.69 \times 10^4$, $\gamma_{\mathrm{max}} = 1.8 \times 10^5$, $q_e = 3.2 \times 10^{-4}$ cm^{-3} s^{-1}, and $s = 1.6$. The dotted line in Figure 4 shows the predicted spectrum obtained by using these analytic values.

This first set of parameters in fact produces much higher luminosities than observations, which is not surprising as explained above. Then we try to search for the best-fit parameters by changing model parameters to match the predictions with observations. Finally, we find a satisfactory set of model parameters to be $\delta = 12$, $R = 2.8 \times 10^{16}$ cm, $B = 0.12$ G, $\gamma_{\mathrm{max}} = 1.5 \times 10^5$, $q_e = 9.6 \times 10^{-6}$ cm^{-3} s^{-1}, and $s = 1.6$. In this fitting procedure, we fix the reference value of s, because s can be determined with little error from the spectral shape of the low-energy synchrotron emission. The thick solid curve in Figure 4 shows the predicted spectrum of Mrk 421 calculated from equations (1) and (3) for the best parameter set given above. The corresponding electron energy spectrum is shown by the thick solid curve in Figure 5. The ratio of u_e/u_B derived using this self-consistent numerical result is $u_e/u_B = 5$.

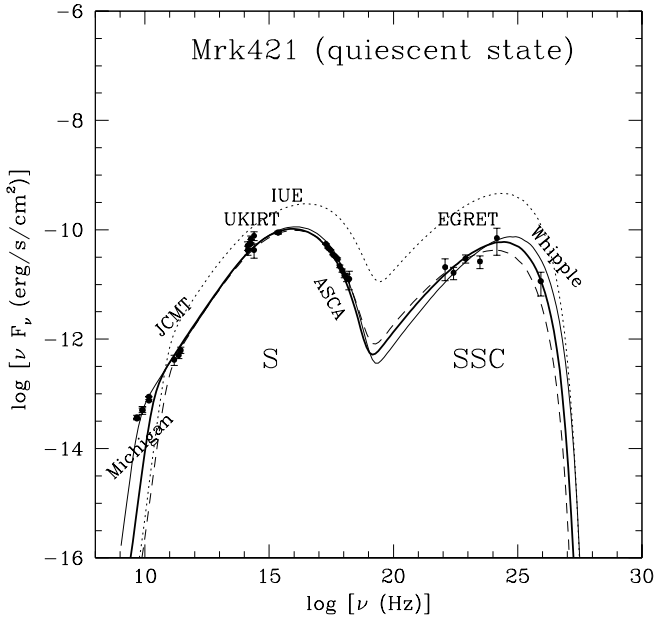

FIG. 4.—One-zone SSC model spectra for the steady state emission of Mrk 421. The thick solid line shows the best-fit spectrum where the adopted parameters are $\delta = 12$, $R = 2.8 \times 10^{16}$ cm, $B = 0.12$ G, $\gamma_{\mathrm{max}} = 1.5 \times 10^5$, $q_e = 9.6 \times 10^{-6}$ cm^{-3} s^{-1}, $s = 1.6$, and $u_e/u_B = 5$. The dotted line shows the spectrum obtained using the analytic estimates for Mrk 421. The thin solid and dashed lines show the spectra of low and high injection models, respectively, to indicate the uncertainty range of the spectral fitting.

The thin solid curve and the dashed curve in Figures 4 and 5 are for different sets of model parameters used to examine the range of uncertainties in the values of the model parameters. The dashed curve is for the case in which

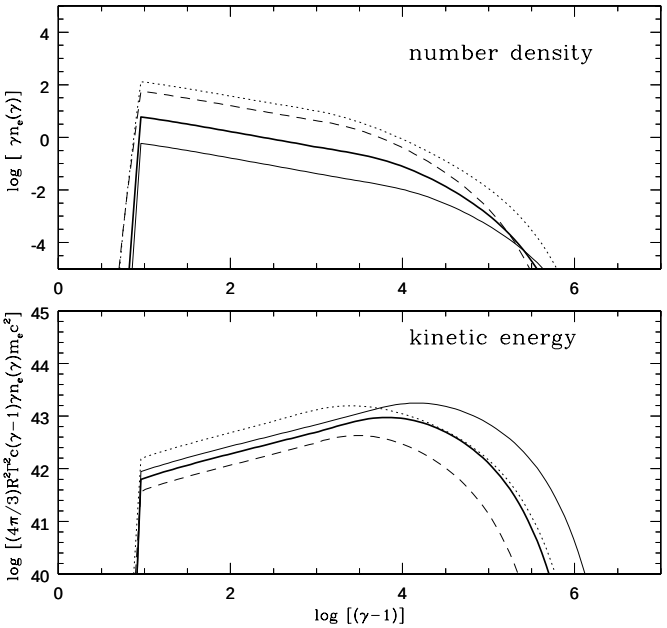

FIG. 5.—Electron energy spectrum and kinetic power of Mrk 421 corresponding to Fig. 4.

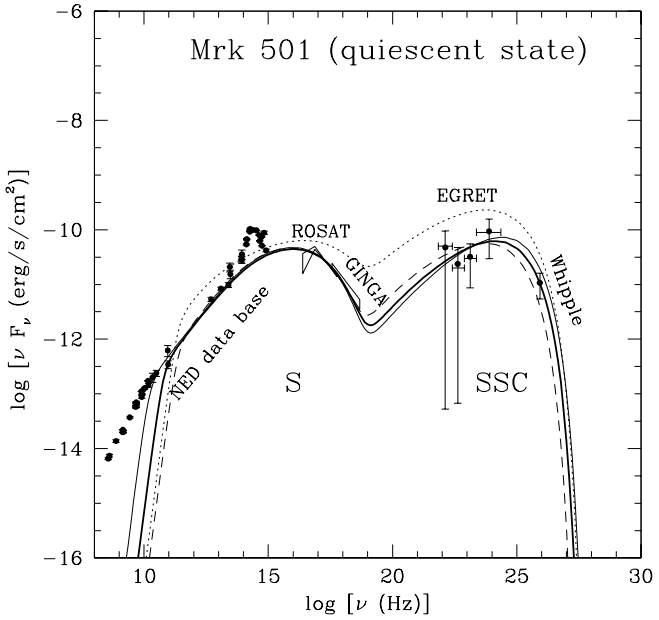

FIG. 6.—One-zone SSC model spectra for the steady state emission of Mrk 501. The thick solid line shows the best-fit spectrum where the adopted parameters are $\delta = 11$, $R = 1.0 \times 10^{16}$ cm, $B = 0.20$ G, $\gamma_{max} = 2.0 \times 10^5$, $q_e = 1.7 \times 10^{-3}$ cm^{-3} s^{-1}, $s = 1.8$, and $u_e/u_B = 22$. The dotted line shows the spectrum obtained using the analytic estimates for Mrk 501. The thin solid and dashed lines show the spectra of low and high injection models, respectively, to indicate the uncertainty range of the spectral fitting.

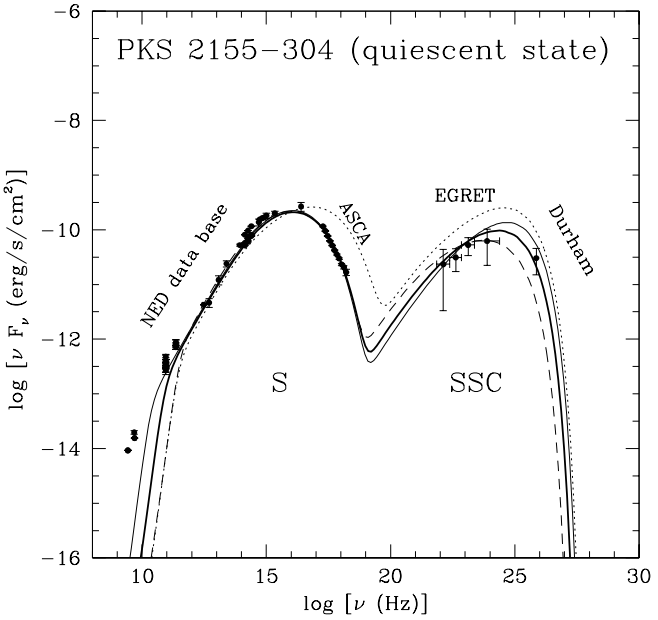

FIG. 8.—One-zone SSC model spectra for the steady state emission of PKS 2155−304. The thick solid line shows the best-fit spectrum where the adopted parameters are $\delta = 33$, $R = 9.0 \times 10^{15}$ cm, $B = 0.30$ G, $\gamma_{max} = 0.5 \times 10^5$, $q_e = 2.8 \times 10^{-5}$ cm^{-3} s^{-1}, $s = 1.4$, and $u_e/u_B = 3$. The dotted line shows the spectrum obtained using the analytic estimates for PKS 2155−304. The thin solid and dashed lines show the spectra of low and high injection models, respectively, to indicate the uncertainty range of the spectral fitting.

q_e is 50 times larger than the best-fit value. The thin solid curve is for the case in which q_e is 50 times smaller than the best-fit value. These two sets of parameters may be regarded as marginally allowed, although the discrepancy in the TeV range is fairly large. The resultant values of the model parameters are tabulated in Table 1. As is seen, for the larger value of q_e, the values of R and γ_{max} become smaller, while the values of B and δ become larger. For a smaller value of q_e, the reverse is true. Table 1 shows the range of uncertainties for model parameters too. In particular, the ratio of u_e/u_B is uncertain by a factor of a few and the dominance of electrons over magnetic field is not changed. The values of δ, γ_{max}, and B are uncertain by factors of about 2, 5, and 10, respectively. The size of the emission region is least constrained with an uncertainty by a factor of 30, but it covers a

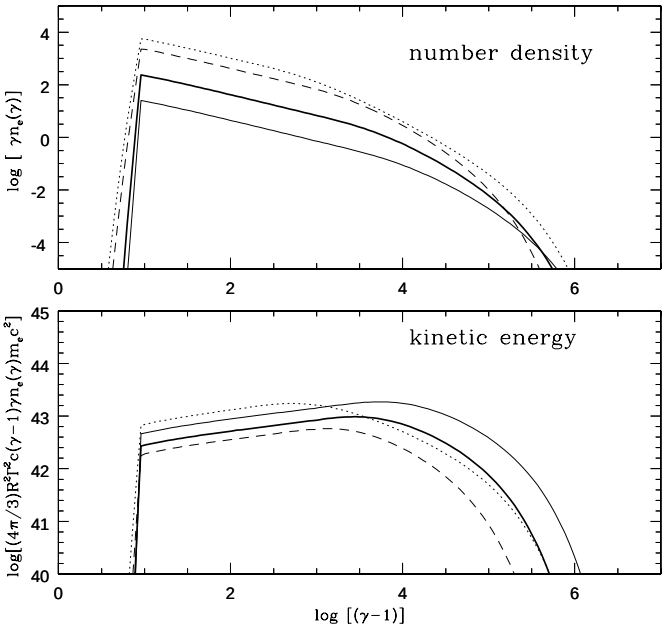

FIG. 7.—Electron energy spectrum and kinetic power of Mrk 501 corresponding to Fig. 6.

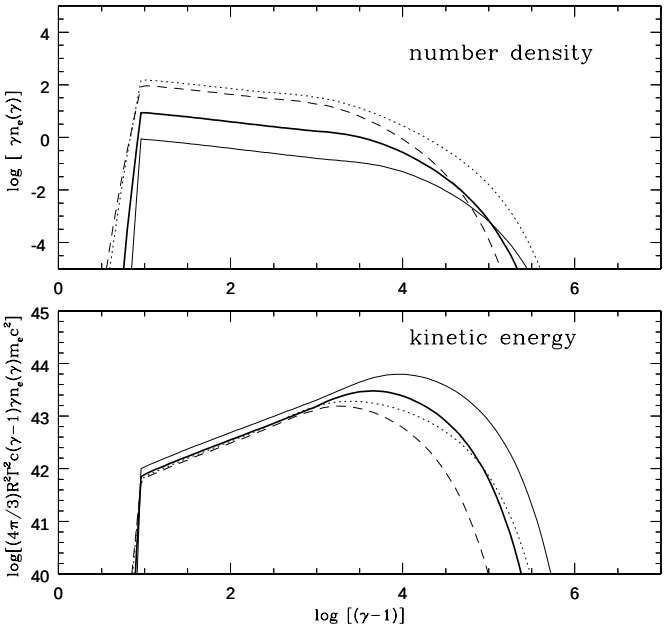

FIG. 9.—Electron energy spectrum and kinetic power of PKS 2155−304 corresponding to Fig. 8.

reasonable range. These results can be roughly understood by combining equations (6), (7), (9), and (11).

4.1.2. *Mrk 501*

BL Lac object Mrk 501 ($z = 0.034$) is also a well-known source of TeV γ-rays detected by the Whipple Cerenkov telescope (Quinn et al. 1996). Observables of Mrk 501 are chosen as follows (Kataoka 2000): $\alpha = 0.4$, $\nu_{\mathrm{syn},o,\mathrm{br}} = 6.3 \times 10^{13}$ Hz, $\nu_{\mathrm{syn},o,\mathrm{max}} = 4.0 \times 10^{17}$ Hz, $\nu_{\mathrm{ssc},o,\mathrm{max}} = 1.0 \times 10^{26}$ Hz, $F_{\mathrm{syn},o} = 3.5 \times 10^{-10}$ ergs cm^{-2} s^{-1}, and $F_{\mathrm{ssc},o} = 4.5 \times 10^{-10}$ ergs cm^{-2} s^{-1}. Substituting these values into the analytic estimate, we obtain $\delta = 10.1$, $R = 3.5 \times 10^{15}$ cm, $B = 0.55$ G, $\gamma_{\mathrm{br}} = 0.31 \times 10^4$, $\gamma_{\mathrm{max}} = 2.5 \times 10^5$, $q_e = 2.4 \times 10^{-2}$ cm^{-3} s^{-1}, and $s = 1.8$.

In a similar way to the case of Mrk 421, we find that a satisfactory fit is obtained for the parameters as $\delta = 11$, $R = 1.0 \times 10^{16}$ cm, $B = 0.20$ G, $\gamma_{\mathrm{max}} = 2.0 \times 10^5$, $q_e = 1.7 \times 10^{-3}$ cm^{-3} s^{-1}, and $s = 1.8$. The thick solid curve in Figure 6 shows the predicted spectrum of Mrk 501 obtained by numerically calculating equations (1) and (3) for the best-fit parameter set given above. The corresponding electron energy spectrum is shown by thick solid curves in Figure 7. The ratio of u_B/u_e derived from this numerical result is $u_e/u_B = 22$.

As is for Mrk 421, the model predictions for the injection rates 50 times higher and lower than the best-fit value are depicted by dashed and thin solid curves in Figures 6 and 7. The numerical values are tabulated in Table 2. Since the trend of uncertainties is the same as for Mrk 421, we do not repeat it here.

4.1.3. *PKS 2155−304*

TeV emission from PKS 2155−304 ($z = 0.117$) was detected very recently by the Durham Mark 6 Cerenkov telescope (Chadwick et al. 1999). Observables of PKS 2155−304 are chosen as follows (Kataoka 2000): $\alpha = 0.2$, $\nu_{\mathrm{syn},o,\mathrm{br}} = 4.0 \times 10^{14}$ Hz, $\nu_{\mathrm{syn},o,\mathrm{max}} = 2.0 \times 10^{17}$ Hz, $\nu_{\mathrm{ssc},o,\mathrm{max}} = 1.0 \times 10^{26}$ Hz, $F_{\mathrm{syn},o} = 1.2 \times 10^{-9}$ ergs cm^{-2} s^{-1}, and $F_{\mathrm{ssc},o} = 5.8 \times 10^{-10}$ ergs cm^{-2} s^{-1}. Substituting these observables into the analytic estimate, we obtain $\delta = 35.5$, $R = 1.9 \times 10^{15}$ cm, $B = 0.89$ G, $\gamma_{\mathrm{br}} = 0.34 \times 10^4$, $\gamma_{\mathrm{max}} = 0.76 \times 10^5$, $q_e = 2.3 \times 10^{-3}$ cm^{-3} s^{-1}, and $s = 1.4$.

In a similar way to the cases of Mrk 421 and Mrk 501, we find that a satisfactory fit is obtained for the parameter set given by $\delta = 33$, $R = 9.0 \times 10^{15}$ cm, $B = 0.3$ G, $\gamma_{\mathrm{max}} = 0.5 \times 10^5$, $q_e = 2.8 \times 10^{-5}$ cm^{-3} s^{-1}, and $s = 1.4$. The thick solid curve in Figure 8 shows the predicted spectrum of PKS 2155−304 by numerically solving equations (1) and (3) for the best parameter set above. The corresponding electron energy spectrum is shown by the thick solid curve in Figure 9. The value of the ratio u_e/u_B turns out to be $u_e/u_B = 3$ for this model parameters.

As is the case for Mrk 421 and Mrk 501, the model predictions for injection rates 50 times higher and lower than the best-fit value are depicted by dashed and thin solid curves in Figures 8 and 9. The numerical values are tabulated in Table 3, and the trend of uncertainties is the same as for Mrk 421 and Mrk 501.

5. SUMMARY AND DISCUSSION

To summarize, within the framework of the one-zone synchrotron self-Compton model, we determined the numerical values of the physical quantities of TeV blazars Mrk 421, Mrk 501, and PKS 2155−304 in quiescent states. Those values are searched for by solving the kinetic equations of electrons and photons taking a proper account of injection, escape, and cooling of electrons and by comparing predicted radiation spectra with observations. The best-fit parameters and uncertainties are estimated. It is shown that the ratio of the energy density of electrons to that of magnetic fields can be determined within a factor of a few, and the ratio is about 5, 22, and 3 for Mrk 421, Mrk 501, and PKS 2155−304, respectively. Thus, the emission region of TeV blazars is particle dominated. For other parameters, δ and γ_{max} are also determined within a factor of a few, while the magnetic field strength and the size have a uncertainties of factors of 10 and 30, respectively. Since these results have important implications for the fundamental understanding of the formation and bulk acceleration of relativistic jets, we discuss below some of the further issues to be explored.

5.1. *u_e/u_B Ratio*

First, we discuss the value of γ_{min} because it is important for determining the u_e/u_B ratio. From a theoretical standpoint, in the case of pair plasma jets, we regard it most likely that $\gamma_{\mathrm{min}} \sim \Gamma$, since the shock first thermalizes a bulk population of particles and then accelerates them from this pool. On the other hand, for the normal electron-proton plasma, there is a wide range of possibilities for γ_{min}. One extreme case is that protons and electrons are separately thermalized, which leads to $\gamma_{\mathrm{min}} \sim \Gamma$. Such a separate thermalization is supposed to be realized for nonrelativistic shocks in supernova remnants. The other extreme case is that electrons and protons attain an equilibrium state, which means $\gamma_{\mathrm{min}} \sim (m_p/m_e)\Gamma$. This picture is conventionally assumed for models of cosmic γ-ray bursts (Sari, Piran, & Narayan 1998). In this case $\gamma_{\mathrm{min}} \sim 10^4$ may be realized, although the real value is likely to be between these two values.

From the observational standpoint, it is also difficult to determine γ_{min}. Since the observed synchrotron frequency from an electron with the Lorentz factor γ_{min} is given by

$$\nu_{\mathrm{syn},o,\mathrm{min}} = 1.2 \times 10^6 B \gamma_{\mathrm{min}}^2 \frac{\delta}{1+z}\,, \tag{34}$$

electrons with $\gamma_{\mathrm{min}} \sim 10$ and 10^4 emit synchrotron photons of $\sim 10^8$ and 10^{14} Hz, respectively, for typical values $B \simeq 0.1$G and $\delta \simeq 10$. The former is well below the self-absorption frequency, and the emission in the low-frequency band is dominated by that from more extended regions. Since the latter frequency is well above the self-absorption, we must modify the model such that emission below 10^{14} Hz is not from the X-ray–emitting one-zone region but from a separate region.

In our one-zone model, to attain the conventional equipartition state of $u_e = u_B$ by simply changing γ_{min} alone, we need to adopt $\gamma_{\mathrm{min}} \sim 1.7 \times 10^4$, 3.2×10^4, and 0.5×10^4 for Mrk 421, Mrk 501, and PKS 2155−304, respectively. It is of some interest that these analytically estimated values are near the value 10^4 mentioned above. For $\gamma_{\mathrm{min}} \sim 10^4$, the predicted spectra around near-infrared and optical bands are difficult to match to the observed data in the one-zone model. In this case, whole synchrotron spectra may be reproduced by a superposition of emission from inhomogeneous jets. An example of this kind of modeling is shown in the recent work of Katarzyński, Sol, & Kus (2001) concerning the broadband spectra of Mrk 501 in the flaring stage by a one-zone SSC blob in a conical jet. The blob explains

X-ray and γ-ray bands, while the jet explains the spectrum from the optical to the radio bands. We note that their u_e/u_B ratio for the blob is similar to ours, irrespective of the actual value of $\gamma_{\rm min}$, for this flaring stage of Mrk 501, although they did not explicitly mention it.

5.1.1. *The Case of* $\gamma_{\rm min} = 10^4$

As discussed above, it is important to examine if the alternative case of $\gamma_{\rm min} \sim 10^4$ and $u_e/u_B \lesssim 1$, for normal plasma can reproduce the high-energy part of the emission spectra in quiescent states.

First, we check the case where $\gamma_{\rm br}$ is still larger than $\gamma_{\rm min}$. The other parameters are fixed as the best-fitting ones obtained in the previous section. The numerical results for Mrk 421 are shown in Figures 10 and 11. As is seen in Figure 10, the low-energy part of both synchrotron and inverse Compton emission is short of the observation. In this case, the numerical value of u_e/u_B turns out to be 2, and yet the emission region is kinetic power dominated. Hence we can rule out the possibility of $u_e/u_B < 1$ for $\gamma_{\rm min} < 10^4$.

The second case is $\gamma_{\rm min} > \gamma_{\rm br}$, for which we analytically examine the expected trend. When $\gamma_{\rm br} < \gamma_{\rm min}$ is satisfied, the electron energy spectrum is given by

$$n_e(\gamma) = \begin{cases} q_e\, t_{e,\rm esc}\, \gamma_{\rm min}^{-s+1}\, \gamma_{\rm br}\, \gamma^{-2} & \text{for } \gamma_{\rm br} \le \gamma < \gamma_{\rm min}\,, \\ q_e\, t_{e,\rm esc}\, \gamma_{\rm br}\, \gamma^{-s-1} & \text{for } \gamma_{\rm min} < \gamma \le \gamma_{\rm max}\,. \end{cases} \quad (35)$$

This regime is called *fast cooling* by Sari et al. (1998) in the models of γ-ray bursts. In this case, instead of equation (28), we obtain

$$\frac{u_e}{u_B} = 9 c_2^{-1} c_3^{-1} \left(1 + \frac{f_{\rm ssc}}{f_{\rm syn}}\right) \frac{f_{\rm ssc}}{f_{\rm syn}} \frac{\gamma_{\rm br}}{\gamma_{\rm min}^{s-1}} \frac{\ln(\gamma_{\rm min}/\gamma_{\rm br})}{\int_{\gamma_{\rm min}}^{\gamma_{\rm max}} \gamma^{-s+1} d\gamma}\,. \quad (36)$$

Since the combinations of the observables $\nu_{{\rm syn},o,{\rm max}}$, $\nu_{{\rm ssc},o,{\rm max}}$, $L_{{\rm syn},o}$, and $L_{{\rm ssc},o}$ are the same as before, from equations (8), (7), and (11), $\delta\gamma_{\rm max}$, $B\delta\gamma_{\rm max}^2$, and $\delta^4 R^2 B^2$ are not changed. From equation (12), $\gamma_{\rm br}$ is proportional to $R^{-1}B^{-2}$ if we neglect Compton cooling. Thus, we obtain $B \propto \delta \propto \gamma_{\rm br}$, $R \propto \gamma_{\rm br}^{-3}$, and $\gamma_{\rm max} \propto \gamma_{\rm br}^{-1}$. From this, we see that stronger cooling, i.e., smaller values of $\gamma_{\rm br}$, implies smaller magnetic field strength and beaming factor and larger size and $\gamma_{\rm max}$. This is not a favorable choice of parameters, because their direction of changes is contradictory to the observational facts about strong beaming and rapid time variability. Therefore, a fast cooling regime is not favored. We thus conclude that our conclusion of kinetic power dominance is fairly robust.

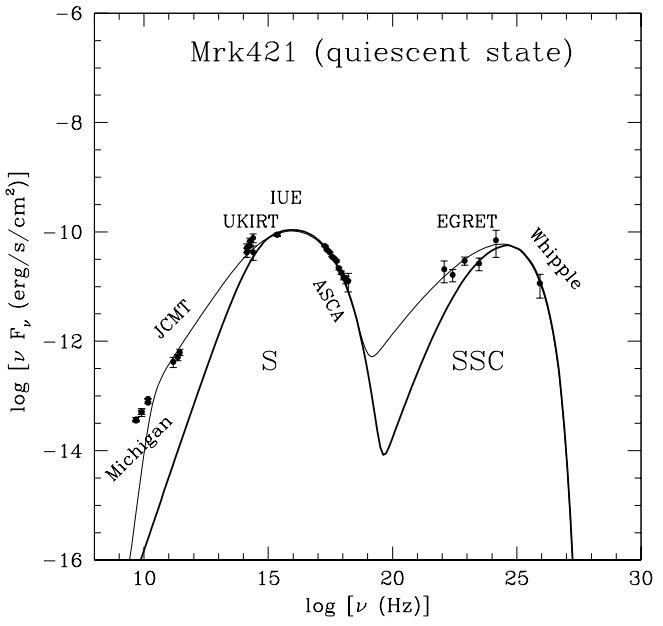

FIG. 10.—One-zone SSC model spectra for the steady state emission of Mrk 421 for $\gamma_{\rm min} = 1 \times 10^4$ and $u_e/u_B = 2$. The thick solid line shows the spectrum for this case; the other parameters are the same as in Fig. 4. The thin solid line shows the best-fit spectrum of Mrk 421 shown in Fig. 4.

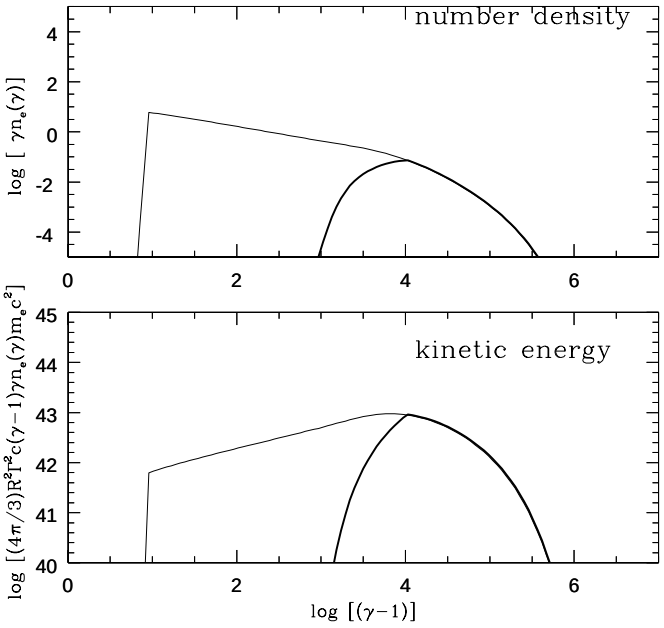

FIG. 11.—Electron energy spectrum and kinetic power of Mrk 421 corresponding to Fig. 10.

5.2. *Proton Components*

It is interesting to know what constraints on the jet material can be obtained from this analysis. Let us assume that the jet consists of relativistic electrons and cold protons and that there are neither thermal electrons nor relativistic protons. Then, using the electron number density for $\gamma_{\rm min} = 10$ and charge neutrality, the kinetic power of cold protons is estimated to be 2.4×10^{44}, 7.8×10^{44}, and 4.0×10^{44} ergs s^{-1}, for Mrk 421, Mrk 501, and PKS 2155−304, respectively. These values are several to 10 times larger than the kinetic power of electrons. This small ratio of the kinetic power of protons to that of electrons, not withstanding the large mass ratio, is due to a large average Lorentz factor of relativistic electrons. Because the proton kinetic power does not exceed the Eddington luminosity for a representative black hole mass in AGNs, we do not make a strong argument about jet material in this way alone. Also, for the case for $\gamma_{\rm min} = 10^4$, proton kinetic power is less than that of relativistic electrons. Estimation of the large-scale kinetic power of these sources can in principle discriminate between these two possibilities, i.e., proton-electron jets or electron-positron jets. Considering the weakness of the extended radio emission of TeV blazars, the same kind of analysis for GeV blazars seems to be more promising. We will analyze GeV blazars in the future.

5.3. *Further Comments*

We discuss the injection index s. For TeV blazars studied in this work, s is smaller than 2. Some recent work has

reported that in Fermi acceleration at ultrarelativistic shocks, s is larger than 2 (Gallant, Achterberg, & Kirk 1999; Kirk et al. 2000), unlike our adopted values based on observed spectra. This is an interesting open question, and we await future research.

As for the ratio of the energy densities of the relativistic electrons to the magnetic fields, what is physically more meaningful may be the ratio $(u_e + u_{\rm rad}/C_3)/u_B$, because this corresponds to the ratio of the injected kinetic power to the Poynting power, while u_e/u_B corresponds to the remaining ratio after radiative cooling. The former ratio becomes 10, 41, and 6 for Mrk 421, Mrk 501, and PKS 2155−304, respectively. Thus, the conclusion does not change much, although it is somewhat strengthened.

In most of the previous work, we also neglected the correction for the absorption of TeV γ-rays due to the CIB. For Mrk 421 and Mrk 501 in quiescent states, this neglect seems safe, if the observed spectra do not extend much over the TeV range. However, for PKS 2155−304 at a redshift of 0.117, the optical depth for 0.35 TeV photons amounts to about 0.5, although the exact value depends on the CIB intensity and spectrum. Thus the intrinsic SSC luminosity of PKS 2155−304 should be a little higher than the estimate given in this paper. Consequently, the ratio u_e/u_B is somewhat higher than the value obtained above, and our conclusion of the kinetic power dominance is strengthened.

Now, we briefly compare our results with the previous work of others. Tavecchio et al. (1998) derived the values of physical parameters in a similar way to our analytical method. However, in their paper, electron energy distribution is not calculated self-consistently. This means that the normalization, index, and $\gamma_{\rm br}$ of relativistic electrons are not derived from solving the cooling and injection processes but obtained only from a fitting of the observed spectrum with a double power-law spectrum. Here we examine the case of Mrk 421, because this is the only source for which multifrequency spectral fitting was done and the number density of the accelerated electrons was estimated by them.

Their best-fit parameters for Mrk 421 are $B = 0.15$ G, $\delta = 25$, and $R = 2.7 \times 10^{15}$ cm, and their electron energy spectrum is given by $n_e(\gamma) = K\gamma^{-n_1}(1 + \gamma/\gamma_{\rm br})^{n_1 - n_2}$, with $n_1 = 2.2$, $n_2 = 4.5$, $\gamma_{\rm br} = 5.6 \times 10^4$, and $K = 1.7 \times 10^5$. Note that they are significantly different from our values. Their electron spectral index of 2.2 is steeper than the value of 1.6 in this work, and it produces a much steeper synchrotron spectrum at low energies. Their estimate of the emission region is more compact and more strongly beamed than ours. Their parameter values correspond to $u_e/u_B = 371$ for a choice of $\gamma_{\rm min} = 10$ and $\gamma_{\rm max} = 10^6$, and the ratio does not much change for different choices of $\gamma_{\rm min}$ and $\gamma_{\rm max}$. Thus, the adopted values by Tavecchio et al. (1998) would mean even more kinetic power dominated states than our results. A major reason for this difference is due to the choice of s, because replacing $s = 2.2$ by $s = 1.6$ leads to $u_e/u_B = 19$.

Although we do not make further comparison with other work, we again emphasize that our method is superior to previous ones in that the break energy of electrons is self-consistently determined and direct spectral fitting is made.

We thank an anonymous referee for useful comments, which helped us to improve this paper. We are grateful to J. Kataoka for kindly providing us with observational data and for useful discussions. This work is supported in part by a Grand-in-Aid from Ministry of Education, Science, Sports and Culture of Japan (11640236, F. T.).

REFERENCES

Aharonian, F., et al. 2001, ApJ, 546, 898
Bednarek, W., & Protheroe, R. J. 1997, MNRAS, 292, 646
Blandford, R. D., & Eichler, D. 1987, Phys Rep., 154, 1
Blandford, R. D., & Königl, A. 1979, ApJ, 232, 34
Blandford, R. D., & Levinson, A. 1995, ApJ, 441, 79
Chadwick, P. M., et al. 1999, ApJ, 513, 161
Comastri, A., Fossati, G., Ghisellini, G., & Molendi, S. 1997, ApJ, 480, 534
Comastri, A., Molendi, S., & Ghisellini, G. 1995, MNRAS, 277, 297
Coppi, P. S., & Blandford, R. D. 1990, MNRAS, 245, 453
Crusius, A., & Schlickeiser, R. 1986, A&A, 164, L16
Dermer, C. D., & Schlickeiser, R. 1993, ApJ, 416, 458
Gaidos, J., et al. 1996, Nature, 383, 319
Gallant, Y. A., Achterberg, A., & Kirk, J. G. 1999, A&AS, 138, 549
Ghisellini, G., & Madau, P. 1996, MNRAS, 280, 67
Hartman, R. C., et al. 1999, ApJS, 123, 79
Hirotani, K., Iguchi, S., Kimura, M., & Wajima, K. 1999, PASJ, 51, 263
Inoue, S., & Takahara, F. 1996, ApJ, 463, 555
Jones, F. C. 1968, Phys. Rev., 167, 1159
Jones, T. W., O'Dell, S. L., & Stein, W. A. 1974, ApJ, 188, 353
Kataoka, J. 2000, Ph.D. thesis, Univ. Tokyo
Kataoka, J., et al. 1999, ApJ, 514, 138
———. 2000, ApJ, 528, 243
Katarzyński, K., Sol, H., & Kus, A. 2001, A&A, 367, 809
Kirk, J. G., Guthmann, A. W., Gallant, Y. A., & Achterberg, A. 2000, ApJ, 542, 235
Kirk, J. G., Rieger, F. M., & Mastichiadis, A. 1998, A&A, 333, 452
Kubo, H., et al. 1998, ApJ, 504, 693
Maraschi, L., Ghisellini, G., & Celotti, A. 1992, ApJ, 397, L5
Mastichiadis, A., & Kirk, J. G. 1997, A&A, 320, 19
Mukherjee, R., et al. 1997, ApJ, 490, 116
Li, H., & Kusunose, M. 2000, ApJ, 536, 729
Punch, M., et al. 1992, Nature, 358, 477
Quinn, J., et al. 1996, ApJ, 456, L83
Reynolds, C. S., Fabian, A. C., Celotti, A., & Rees, M. J. 1996, MNRAS, 283, 873
Robinson, P. A., & Melrose, D. B. 1984, Australian J. Phys., 37, 675
Rybicki, G. B., & Lightman, A. P. 1979, Radiative Processes in Astrophysics (New York: John Wiley & Sons)
Sari, R., Piran, T., & Narayan, R. 1998, ApJ, 497, L17
Sikora, M., Begelman, M. C., & Rees, M. J. 1994, ApJ, 421, 153
Takahara, F. 1997, Relativistic Jets in AGNs, ed. M. Ostrowski, M. Sikora, G. Madejski & M. Begelman (Krakow: Jagellonian Univ.), 253
Tavecchio, F., Maraschi, L., & Ghisellini, G. 1998, ApJ, 509, 608
Urry, C. M., & Padovani, P. 1995, PASP, 107, 803
von Montigny, C., et al. 1995, ApJ, 440, 525
Wardle, J. F. C., Homan, D. C., Ojha, R., & Roberts, D. H. 1998, Nature, 395, 457